Numerical study of flow past an elliptic cylinder near a free surface

Rahul Subburaj, Prashant Khandelwal, and S. Vengadesan

Citation: Physics of Fluids **30**, 103603 (2018); doi: 10.1063/1.5046745
View online: https://doi.org/10.1063/1.5046745
View Table of Contents: http://aip.scitation.org/toc/phf/30/10
Published by the American Institute of Physics

Articles you may be interested in

Flow past a circular cylinder executing rotary oscillation: Dimensionality of the problem
Physics of Fluids **30**, 093602 (2018); 10.1063/1.5046474

Hydrodynamic characteristics of flow past a square cylinder at moderate Reynolds numbers
Physics of Fluids **30**, 104107 (2018); 10.1063/1.5050439

Flow-induced oscillation of a rigid rectangular plate hinged at its leading edge
Physics of Fluids **30**, 063601 (2018); 10.1063/1.5026307

Study of the thrust–drag balance with a swimming robotic fish
Physics of Fluids **30**, 091901 (2018); 10.1063/1.5043137

Identification of coherent structures in the flow past a NACA0012 airfoil via proper orthogonal decomposition
Physics of Fluids **29**, 085104 (2017); 10.1063/1.4997202

Normal stress differences from Oldroyd 8-constant framework: Exact analytical solution for large-amplitude oscillatory shear flow
Physics of Fluids **29**, 121601 (2017); 10.1063/1.4994866

PHYSICS TODAY
WHITEPAPERS

ADVANCED LIGHT CURE ADHESIVES

Take a closer look at what these environmentally friendly adhesive systems can do

READ NOW

PRESENTED BY
MASTERBOND

Numerical study of flow past an elliptic cylinder near a free surface

Rahul Subburaj, Prashant Khandelwal, and S. Vengadesan[a)]
Department of Applied Mechanics, IIT Madras, Chennai, India

(Received 1 July 2018; accepted 26 September 2018; published online 18 October 2018)

Flow past an elliptic cylinder near a free surface at a Reynolds number of 180 is studied numerically by varying parameters such as the angle of attack (AOA), aspect ratio (AR), submergence depth (h_S), and Froude number (Fr). The immersed boundary method and level set method are used to study the flow. Simulations are performed for elliptic cylinders with angles of attack varying as −45°, 45°, and 90° and aspect ratios 2 and 4. A detailed investigation of quantities like the Strouhal number and forces provides an understanding on the complex flow interactions between the free surface and the elliptic cylinder of varying AOA and AR. Variation in the angle of attack brings substantial changes in the flow and vortex shedding pattern. The most significant of all changes observed with different AOAs is related to vortex shedding suppression at a depth of 0.096. Vortex shedding is suppressed at an AOA = 45°, but at −45°, metastable states appear, and at 90°, partial vortex shedding suppression occurs. Varying AR, on the other hand, does not bring any significant changes in the flow features, except for variation in mean forces and the Strouhal number. *Published by AIP Publishing.*
https://doi.org/10.1063/1.5046745

I. INTRODUCTION

Understanding the flow behind a bluff body, preferably a circular cylinder, has been the subject of interest to scientists and engineers. Due to its engineering significance, flow past a circular cylinder has been thoroughly studied covering an extensive range of parameters. However, flow past a bluff body near a free surface has been studied in relatively few instances in-spite of its potential applications in submarines, offshore structures, and tidal power generation. Miyata *et al.*[1] investigated, both experimentally and numerically, the flow past a circular cylinder near a free surface at Re = 5000 and Fr = 0.24. They observed a sudden reduction in drag and increase in the Strouhal number when the submergence depth is decreased. Triantafyllou and Dimas[2] analyzed the stability of flow past a half-submerged cylinder and observed that the wake was convectively unstable. Sheridan *et al.*[3] conducted a series of experiments for the flow past a fully submerged circular cylinder at moderately high Re (5000-6000) and Froude numbers ranging from 0.47 to 0.72. Their experiments revealed the existence of two metastable states, viz., the first state, where the jet generated above the cylinder stays attached to the free surface, and second state, where the jet separates from the free surface and flows into the rear portion of the cylinder. Transition between these two states is slower than the time-period of von Kàrmàn shedding.

Reichl *et al.*[4] computed flow past a circular cylinder at a low Reynolds number (Re = 180) and found that their results matched with the experiments performed by Sheridan *et al.*[3] despite the difference in the Reynolds number by a factor of 40. After establishing that the free surface phenomena are only dependent on the submergence depth and Froude number, they examined the effect of the free surface on flow phenomena like vortex shedding, wake instability, wave breaking, etc. The transition between the two metastable states was suggested to be controlled by a feedback loop that constituted of the generation and suppression of wake instability and the role of surface vorticity in controlling the vortex formation from the top shear layer. Bouscasse *et al.*[5] increased the range of the parameter study (submergence depths and Froude numbers) and observed the recovery of vortex street instability with an increase in the global Froude number to 2. This problem is similar to flow past a circular cylinder near a rigid wall,[6–13] but only at a lower Froude number. It is apparent from the above mentioned studies that dominant focus has been on circular cylinders near a free surface. But an elliptic cylinder possesses the ability to manipulate the aerodynamic forces acting on it by changing its angle of attack (AOA). As it has various applications in wings, missiles, and heat exchanger tubes, these studies should be carried out for elliptic cylinders. Elliptic cylinders are shown to alter the flow and vorticity around them when impulsively started[14–16] and at a low Reynolds number.[17,18] Johnson *et al.*[19,20] noted the vorticity dynamics and frequencies in the flow past an elliptic cylinder oriented at 90°. They observed different vortex shedding patterns for varying Reynolds numbers and aspect ratios. Paul *et al.*[21,22] studied flow phenomena like laminar separation, vortex shedding, boundary layers, and thermal wakes for elliptic cylinders of varying AOA and aspect ratio (AR). The free surface also affects the vorticity induced from the bluff body and the average velocity on top of the cylinder, as shown in the work of Reichl *et al.*[4] These observations indicate that flow past an elliptic cylinder will change substantially when it is near the free surface. One of the few experimental studies that analyzed an elliptic cylinder with a free surface was performed by Daichin and Lee,[23] but the cylinder's orientation is limited to 0°. Very few studies have been conducted on flow past an elliptic cylinder of varying AOA and AR near the free surface. Our intent is to provide

[a)]Author to whom correspondence should be addressed: vengades@iitm.ac.in

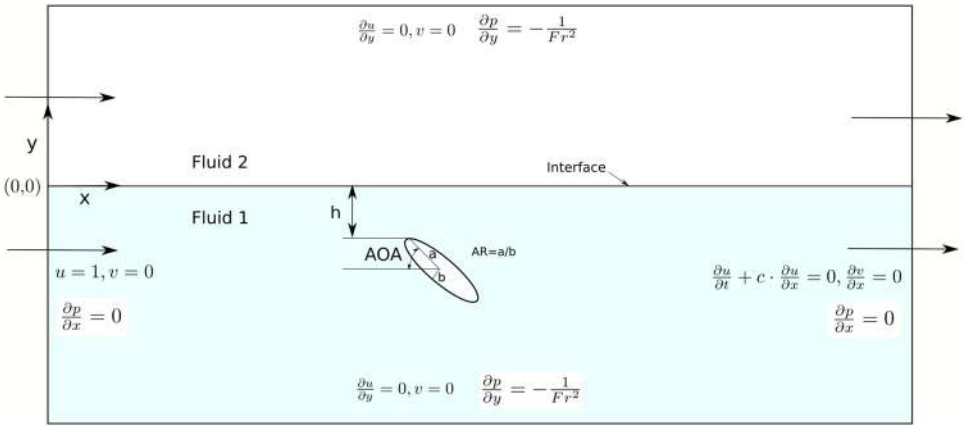

FIG. 1. Schematic of the problem statement.

some insight on this largely unexplored area. In the present work, we investigate flow past an elliptic cylinder of varying AOA and AR near a free surface and analyze flow patterns as well as bulk parameters like aerodynamic forces and the Strouhal number.

II. PROBLEM STATEMENT

Flow past an elliptic cylinder near the free surface is studied by varying the submergence depth (h_S), Froude number (Fr), angle of attack (AOA), and aspect ratio (AR). The angle of attack (AOA) of an elliptic cylinder, denoted by α, is defined as the angle made by the major axis with the incoming flow. The aspect ratio (AR) is defined as the ratio of the major axis and minor axis lengths, and submergence depth is defined as the distance between the top-most point on the cylinder and the interface. As the forces acting on the body are dependent on the surface area or perimeter, the perimeter is kept constant for all the elliptic cylinders and considered as the reference length (Ref. 24). The dimensionless numbers are defined as follows:

$$Re_S = \frac{US}{\nu}, \; Fr = \frac{U}{\sqrt{gS}}, \text{ and } h_S = \frac{h}{S},$$

where U is the reference velocity, S is the perimeter of the body, ν is the kinematic viscosity of Fluid 1 (water), g is the acceleration due to gravity, and h is the minimum distance of the body from the interface, as shown in Fig. 1. When diameter (or apparent diameter) is considered as the reference length, the quantities stated above are expressed as Re_D and Fr_D,

$$Re_D = \frac{UD}{\nu}, \; Fr_D = \frac{U}{\sqrt{gD}},$$

where the apparent diameter is calculated using the relation, $D = S/\pi$. AOA takes values $-45°$, $45°$, and $90°$, while AR takes 2 and 4. The Reynolds number (Re_S) of the flow is kept constant at 565 (Re_D = 180). This Reynolds number is suggested by Reichl *et al.*,[4] in which it is shown that the flow features at a moderately high Reynolds number can be reproduced at a relatively low Reynolds number (Re = 180). Parameters used to carry out these investigations are provided in Table I.

TABLE I. Set of parameters investigated in the study.

Set#	AOA	h_S	Fr
1	−45°, 45°, 90°	0, 0.0478, 0.096, 0.143, 0.191, 0.255, 0.338	0.318
2	−45°, 45°, 90°	0.171	0.169, 0.226, 0.282, 0.451, 0.564, 0.667

III. NUMERICAL METHODOLOGY

A PETSc (Portable Extensible Toolkit for Scientific Computation) based C++ code PetIBM,[25] which utilizes the immersed boundary method to account for the presence of a body in fluid flow, is implemented with a level set method to track the interface. Immersed boundary methods[26–28] can simulate deforming bodies on a non-body conforming grid with ease.

A. Level set method

The level set method, introduced by Sethian,[29] is used to track the water-air interface. The standard level set function is defined to be a signed distance function

$$\phi(x) = \min_{x_I \epsilon I}(|x - x_I|), \tag{1}$$

where ϕ is the level set function and I is the interface. This function takes positive values in the region outside the interface, negative values inside, and zero on the interface. Hence, the zero level set of ϕ moves along with the interface when the following hyperbolic scalar transport equation is solved:

$$\phi_t + \mathbf{u} \cdot \nabla\phi = 0, \tag{2}$$

where $\mathbf{u}$ is the velocity vector. Fifth order weighted essentially non-oscillatory (WENO[30]) schemes are used to discretize the equation in space, and third order total variation diminishing Runge-Kutta (TVDRK3) method in time. Even though the interface ($\phi = 0$) is updated using higher order schemes, ϕ does not remain as a distance function. This often results in steepening of the gradient of ϕ and then in a volume conservation defect. To deal with this problem, ϕ is reinitialized once every 10th iteration, in which an intrinsic property of the level set function $|\nabla\phi| = 1$ is conserved explicitly as specified by Sussman *et al.*[31] by solving the following equation:

$$\phi_t = S(\phi_0) \cdot (1 - |\nabla\phi|), \tag{3}$$

where

$$S(\phi_0) = \phi_0 / \sqrt{\phi^2 + (\epsilon\Delta x)^2}. \tag{4}$$

B. Fluid flow solver

In our study, we calculate the flow field of two immiscible incompressible fluids (water-air) in the presence of a solid body. If the reference density and viscosity used are of Fluid 1 (water), the non-dimensionalized Navier-Stokes equation is given by

$$\frac{\partial \mathbf{u}}{\partial t} + \mathbf{u} \cdot \nabla \mathbf{u} = -\frac{\nabla p}{\rho_r(\phi)} + \frac{\nabla \cdot (\mu_r(\phi)(\nabla \mathbf{u} + \nabla \mathbf{u}^T))}{\rho_r(\phi) Re} + \frac{f_b L}{\rho_r(\phi) U^2} - \frac{\hat{j}}{Fr^2}, \tag{5}$$

$$\nabla \cdot \mathbf{u} = 0, \tag{6}$$

where $\mathbf{u}$ is the velocity vector, p is the pressure, ρ_r is the density ratio (ρ/ρ_1), μ_r is the viscosity ratio (μ/μ_1), f_b is the force that couples fluid motion with the solid body, L is the reference length, and U is the reference velocity with $Re = \frac{\rho_1 LU}{\mu_1}$, $Fr^2 = \frac{U^2}{gL}$ as the dimensionless numbers. ρ and μ are the variable density and viscosity. Density and viscosity ratios are assumed to vary as a smooth Heaviside function,

$$\rho_r(\phi) = 1 + \left(\frac{\rho_2}{\rho_1} - 1\right) H(\phi), \tag{7}$$

$$\mu_r(\phi) = 1 + \left(\frac{\mu_2}{\mu_1} - 1\right) H(\phi). \tag{8}$$

The definition of the smooth Heaviside function is

$$H(\phi) = \begin{cases} 0, & \phi < -\epsilon, \\ \frac{1}{2}(1 + \phi/\epsilon - 1/\pi \sin(\pi\phi/\epsilon)), & |\phi| \le \epsilon, \\ 1, & \phi > \epsilon, \end{cases}$$

with $\epsilon = 1.5\Delta x$. The solid-fluid coupling is achieved using the immersed boundary projection method (IBPM), formulated by Taira and Colonius,[27] wherein the Navier-Stokes equation is written as

$$\begin{pmatrix} A & Q \\ Q^T & 0 \end{pmatrix} \begin{pmatrix} q^{n+1} \\ \lambda \end{pmatrix} = \begin{pmatrix} r_1 \\ r_2 \end{pmatrix},$$

$$\lambda \equiv \begin{pmatrix} \phi \\ \tilde{f} \end{pmatrix}, \; r_1 \equiv r^n + bc_1, \; r_2 \equiv \begin{pmatrix} -bc_2 \\ u_B^{n+1} \end{pmatrix},$$

where q^{n+1} and ϕ are the velocity flux and pressure vectors, respectively. With the operator splitting, we obtain

$$Aq^* = r_1, \tag{9}$$

$$Q^T B^N Q\lambda = Q^T q^* - r_2, \tag{10}$$

$$q^{n+1} = q^* - B^N Q\phi. \tag{11}$$

The terms A, r_1, and B^N are dependent on the density and viscosity. The system of equations are solved using a PETSc[32] based C++ code named PetIBM.[25] Details about the code's implementation and parallelization are presented in the work of Srinidhi and Vengadesan.[25] PETSc provides various solvers and preconditioners to solve PDEs. We have used the GMRES[33] (generalized minimal residual) method as the solver and GAMG[34] (Geometric-Algebraic Multigrid) method as the preconditioner. The simulations are performed using 16 cores ($2 \times$ Intel E5-2670 8 C 2.6 GHz Processor), and the tolerance for solving Eqs. (9) and (10) is 10^{-6}. The total computational time taken for solving in a 2000×340 grid for 10^5 time steps is 1.09×10^5 s, and the average number of iterations taken in a single time step is 7.

IV. VALIDATION

PetIBM has been validated against standard benchmark cases in the work of Srinidhi and Vengadesan.[25] The level set solver implemented along with PetIBM is validated for (1) Rayleigh-Taylor instability, (2) bubble rising in a column, and (3) flow past a submerged circular cylinder.

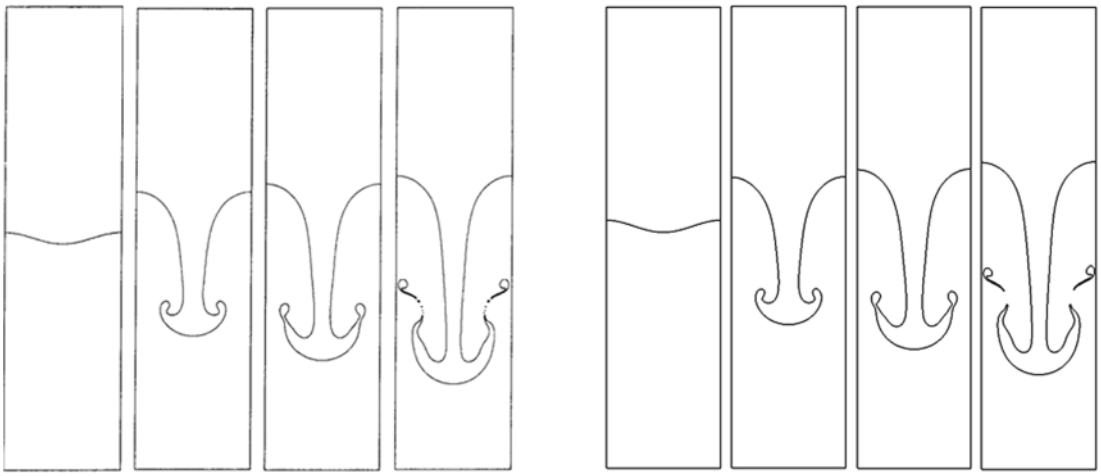

FIG. 2. Qualitative comparison of Rayleigh-Taylor instability at time instants t = 0.1, 0.7, 0.8, and 0.9 s. (a) From the work of Popinet *et al.*[35] and (b) present Simulation.

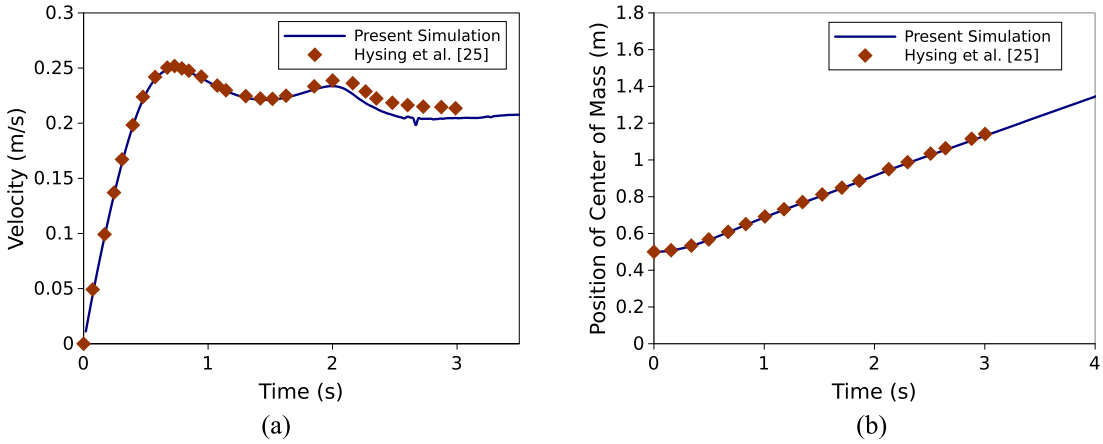

FIG. 3. (a) Velocity and (b) position of the bubble's center of mass (CM).

A. Rayleigh Taylor instability

Rayleigh Taylor instability manifests when a heavier fluid falls onto a lighter fluid under the action of gravity, resulting in a mushroom cone structure. The flow is two-dimensional and a standard benchmark case for multiphase solvers. The parameters used are:
$\rho_2/\rho_1 = 10$, $\mu_2/\mu_1 = 1$, Weber number $= \rho_1 u^2 L/\sigma = 126.70$, Reynolds number $= \rho_1 uL/\mu_1 = 54$, Froude number $= u/\sqrt{gL} = 3.16$, domain size $= 1 \times 4$ m^2, and mesh size $= 50 \times 200$, as specified in the work of Popinet and Zaleski.[35] The results are in good agreement with that of Popinet and Zaleski[35] except for the presence of tiny droplets in the last frame, as shown in the Fig. 2. This is expected as the level set method tends to dissipate droplets that occupy few grid cells.

B. Bubble rising in a column

A bubble of density 1 ($\rho_1 = 1$) rises in a column filled with a heavier fluid of density 1000 ($\rho_2 = 1000$). The viscosity ratio is 100, $Re = uD/\nu_1 = 35$, $We = \rho_1 u^2 D/\sigma = 125$, $Fr = u/\sqrt{gD} = 1$, mesh size $= 128 \times 256$, and cell size $= 1/64$. The velocity and position of the center of mass (CM) of the bubble are determined after the completion of simulation. The results are compared with that of Hysing *et al.*,[36] as shown in Fig. 3. The velocity of CM matches well with the benchmark. The deviation (4.8%) near the second maxima could be attributed to the difference in the interface capturing method itself. Hysing *et al.*[36] use the volume of fluid (VOF) method. Secondary bubbles start detaching earlier compared to our simulation. At time t = 3 s, sizes of the secondary bubbles present in Fig. 4 are different. This

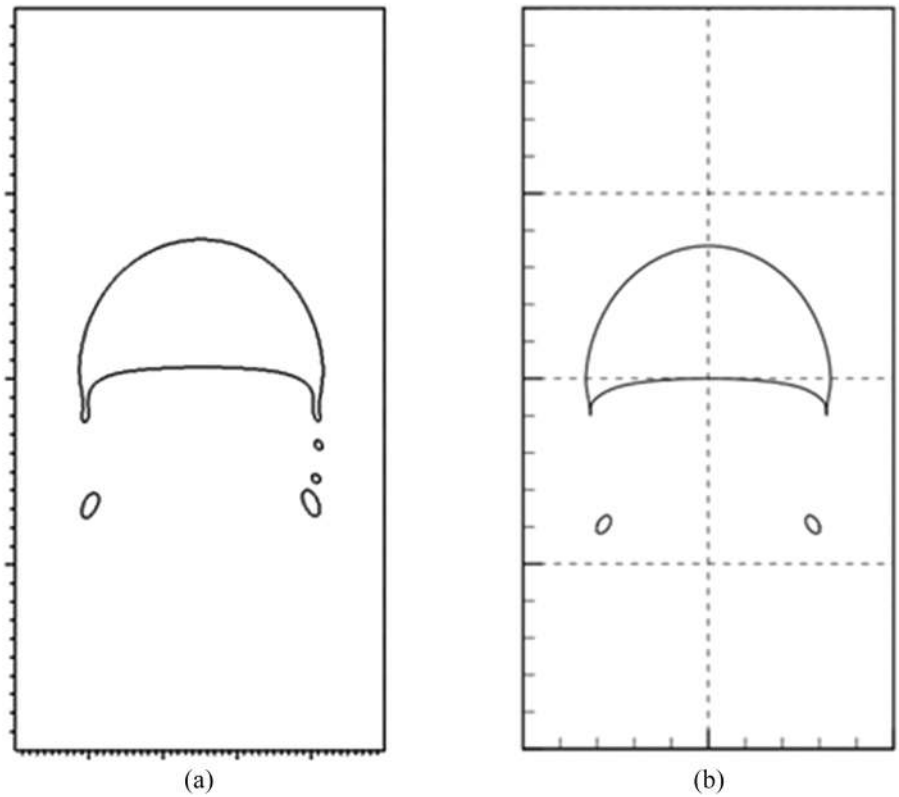

FIG. 4. Qualitative comparison of a bubble at $t = 3s$. (a) Present Simulation and (b) from the work of Hysing *et al.*[36]

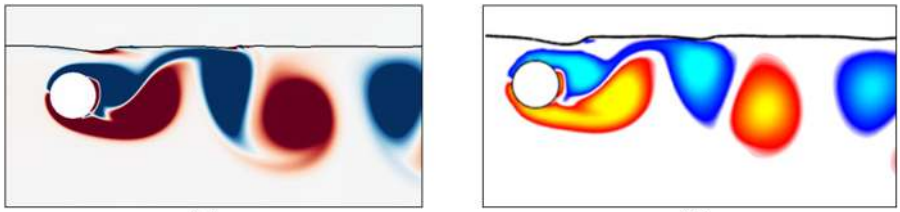

FIG. 5. Vorticity patterns (−3 to 3) for Re = 180, Fr = 0.3, and h/D = 0.55. (a) Present Simulation and (b) from the work of Gubanov.[37]

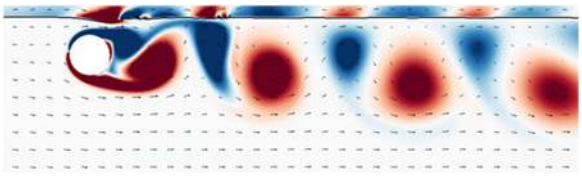

FIG. 6. Vorticity plot at tU/L = 20, Fr = 0.3, h/D = 0.4, and Re = 180.

establishes the difference in the velocity of CM after its second maxima.

C. Flow past a submerged circular cylinder

A circular cylinder is submerged in a fluid of density $\rho = 1000$. The flow parameters are submergence depth h/D = 0.55, Froude number Fr = 0.3, and Reynolds number Re = 180. The results are compared qualitatively with that of Gubanov.[37] The vorticity patterns match well, as shown in Fig. 5.

Next we validate against flow past a submerged cylinder with the parameters h/D = 0.4, Fr = 0.3, and Re = 180 (Fig. 6). Values of the local Froude number Fr_L and average velocity on top of the cylinder at an instant of maximum lift, $\bar{u}_m$, obtained from the simulation and literature are compared in Table II. The values agree well with those of Reichl *et al.*[4] All these validations confirm that further investigations can be carried out using the developed code.

TABLE II. Comparison of results.

Cases	Fr_L	$\bar{u}_m$
Reichl *et al.*[4]	0.73	1.34
Present	0.74	1.32

V. COMPUTATIONAL GRID

For the study on the interaction of flow with an elliptic cylinder, the inflow boundary condition is $u = 1$, $v = 0$; the outflow boundary condition is $\frac{\partial u}{\partial t} + c \cdot \frac{\partial u}{\partial x} = 0$, $\frac{\partial v}{\partial x} = 0$; and the top and bottom boundary condition is $\frac{\partial u}{\partial y} = 0, v = 0$. The pressure boundary conditions are $\frac{\partial p}{\partial x} = 0$ in left and right boundaries and $\frac{\partial p}{\partial y} = -\frac{1}{Fr^2}$ in bottom and top boundaries, as depicted in Fig. 1.

A. Domain independence study

The domain independence study is carried out for flow past a circular cylinder near the free surface with parameters $h/D = 0.55$, $Fr = 0.3$, $\rho_1/\rho_2 = 816$, and $\mu_1/\mu_2 = 64$. Following three domains are chosen for the study:

Domain 1 ($-8 \le x \le 8$, $-5 \le y \le 5$);
Domain 2 ($-10 \le x \le 10$, $-10 \le y \le 10$); and
Domain 3 ($-12.5 \le x \le 12.5$, $-10 \le y \le 10$).

A uniform grid is located in the limits $-1 \le y \le 1$ for all domains with a spacing $\Delta x = 0.01$. As per the restrictions for discretization of the body set in IBM, 81 Lagrangian points are used to discretize the elliptic cylinder. Values of lift and drag coefficients (C_L and C_D) are plotted in Fig. 7. Mean C_L and C_D are compared in Table III. The variation in mean C_L and C_D of Domain 2 from Domain 3 is less than 0.1%. It can be concluded that Domain 2 is large enough to simulate flow free of domain dependence errors.

B. Grid independence study

Domain 2 ($-10 \le x \le 10$, $-10 \le y \le 10$), obtained from the previous study, is used to perform the grid independence

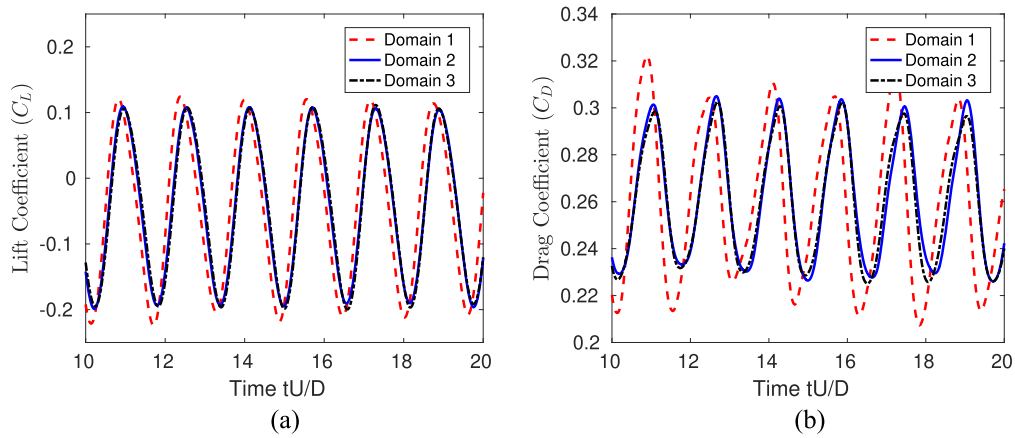

FIG. 7. Domain independence study. (a) C_L and (b) C_D.

TABLE III. Domain independence study.

Domain size	Mean C_L	Mean C_D
$-8 \le x \le 8, -5 \le y \le 5$	−0.048 1	0.2590
$-10 \le x \le 10, -10 \le y \le 10$	−0.047 17	0.2610
$-12.5 \le x \le 12.5, -10 \le y \le 10$	−0.047 22	0.2609

TABLE IV. Grid independence study.

Grid spacing	Mean C_L	Mean C_D
$\Delta x = 0.01$	−0.047 17	0.2610
$\Delta x = 0.008$	−0.047 06	0.2600

study. The study is performed on two grids of different uniform grid spacing, $\Delta x = 1/100$ and 1/125. C_L and C_D on different grids are plotted in Fig. 8. Variation in mean C_L and C_D for Grid 1 from Grid 2 is 0.2% (Table IV). As a result, $\Delta x = 1/100$ is chosen as an appropriate uniform grid spacing for all the simulations.

Finally, a rectangular grid of size $-10 \le x \le 10$, $-10 \le y \le 10$ is chosen as shown in Fig. 1. A small area consisting of a uniform grid ($-10 \le x \le 10$, $-1 \le y \le 1$) with size $\Delta x = 0.01$ is imposed to represent the interface and body.

VI. RESULTS AND DISCUSSION

Before proceeding with our study, an overview of flow past an elliptic cylinder of varying AOA and AR is helpful. An elliptic cylinder at an AOA of 90° possesses the maximum blockage, and vortex shedding occurs in different regimes, as described in the work of Johnson.[19] At this AOA, Radi *et al.*[38] observed that the aspect ratio also affects the cylinder wake and frequency of vortex shedding. In an infinite domain, flow past elliptic cylinders with $\alpha = 45°$ and $-45°$ is expected to be mirror images of each other, thus resulting in equal and opposite lift forces. But the presence of free surface alters the flow substantially, as depicted in Fig. 9. It is observed in Fig. 9(a) that the vortices shed from an elliptic cylinder with $\alpha = -45°$ and $h_S = 0.318$ travel at an angle away from the free surface, while at $\alpha = 45°$ and the same depth [Fig. 9(b)], the vortices stay close to the free surface. The same behavior is observed at low Froude numbers ($Fr = 0.169$), but the angle of shedding is reduced in both the cases. Considering these observations as a rough estimate of differences between flow past an elliptic cylinder of varying AOA and AR, we study the effect of the free surface on cylinder's wake characteristics and the bulk properties.

A. Flow and vortex dynamics

In this subsection, elliptic cylinders of varying AOA and constant AR = 2 are considered for examination at different submergence depths and Froude numbers, as specified in Sec. II. The simulations are run until non-dimensional time tU/S = 100 (tU/D = 300). Figures 10 and 11 show the time series of C_L and C_D for elliptic cylinders with AR = 2 at different submergence depths and AOA. The lift amplitude reduces when the bluff body is moved closer to the free surface irrespective of AOA. The vorticity contours for flow past elliptic cylinders oriented at 45°, −45°, and 90° varying with the submergence depth and Froude number are plotted in Figs. 12 and 13, respectively. These plots help us understand the flow characteristics and infer its effects on the bulk parameters.

1. Angle of attack = −45°

When an elliptic cylinder is placed at $\alpha = -45°$ and $h_S = 0.318$, the vortices shed from the cylinder move as pairs. Even though the effect of the free surface is reduced, it is enough to cause the vortex pairs to move at a certain angle. As the cylinder is moved closer ($h_S = 0.191$) to the free surface, the positive vorticity induced from the free surface intensifies and abets the stretching and diffusion of negative vorticity (from the cylinder). As a result, the vortex pair rotates in the counter-clockwise direction. Negative vorticity of the vortex pair reaches the end of the shear layer present behind the cylinder and gains velocity higher than that of positive vorticity. The amplitude of oscillations in forces, C_L and C_D, reduces due to this weakening of negative vorticity. With the further reduction in submergence depth ($h_S = 0.096$), negative vorticity diffuses faster and the force amplitude reduces even more. At this h_S, we notice the existence of metastable states, which brings varying amplitudes in C_L. Nevertheless it is smaller in comparison with amplitudes at higher h_S. The mechanism behind its transition is stated in the work of Reichl *et al.*[4] Finally when the cylinder touches the free surface [Fig. 12(a)], vortex shedding is suppressed and negative vorticity is absent in the wake as the flow above the cylinder is completely restricted. A large recirculation zone is observed, with the source being the shear layer emanating from the bottom surface of the cylinder. The reduction in the amplitude of C_L with decreasing h_S (Fig. 10)

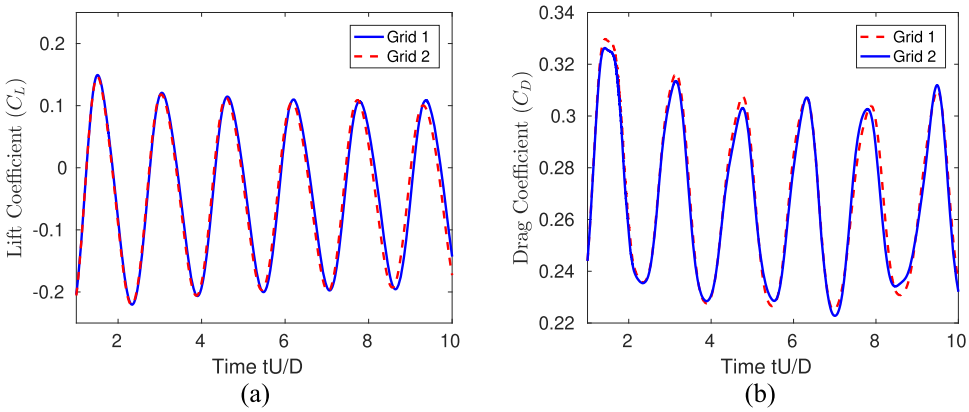

FIG. 8. Grid independence study. (a) C_L and (b) C_D.

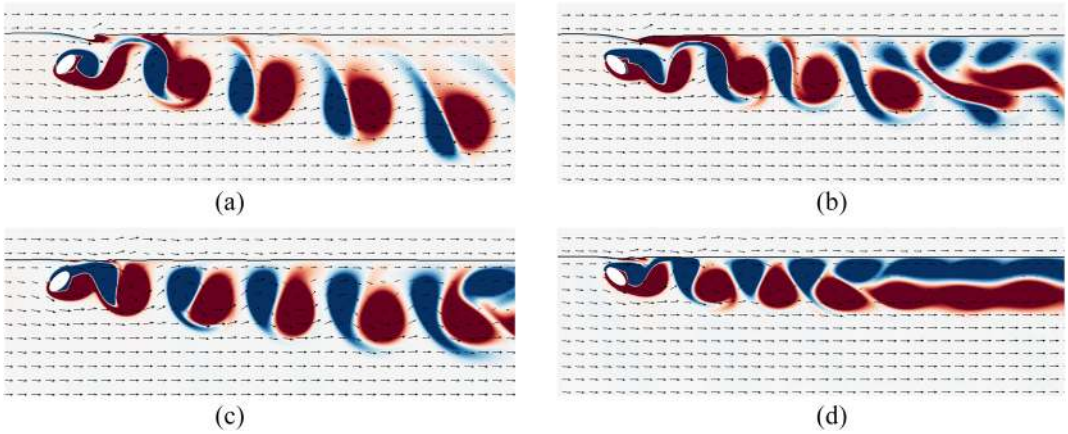

FIG. 9. Vortex shedding patterns at tU/S = 60 for different AOAs. (a) $\alpha = -45°$, $h_S = 0.318$, $Fr = 0.338$; (b) $\alpha = 45°$, $h_S = 0.318$, $Fr = 0.338$; (c) $\alpha = -45°$, $h_S = 0.175$, $Fr = 0.169$; and (d) $\alpha = 45°$, $h_S = 0.175$, $Fr = 0.169$.

is because of the free surface's stabilizing effect. The positive vorticity induced from the free surface helps in the diffusion of negative vorticity. Stabilization of the wake is also observed with increasing Froude number. When the Froude number is increased (Fig. 13), the flow feature changes from vortex shedding ($Fr = 0.169$) to its suppression ($Fr = 0.667$) resulting in a stable jet emanating from the top surface of the cylinder. At Froude number $Fr = 0.226$, we observe irregular vortex shedding in which the negative vorticity splits into two parts: one far away and other near the free surface. The former moves faster than the latter due to the presence of the shear layer behind the cylinder. At a slightly higher Froude number $Fr = 0.451$, the blobs that existed near the free surface in the previous case ($Fr = 0.226$) vanish completely.

2. Angle of attack = 45°

Stabilization of flow is observed at $\alpha = 45°$ with decreasing depths and increasing Froude numbers, similar to that in the previous AOA case. But, the amplitude of C_L for $\alpha = 45°$ is the minimum amongst all AOAs at all submergence depths and Froude numbers, as seen in Fig. 10. There are major differences in the fluid characteristics too. Vortex shedding is observed but with the vortices shed close to the free surface at a depth of $h_S = 0.318$. The negative vorticity undergoes stretching, and it separates into two blobs, one far away from the free surface speeding up and the other near slowing down. With the reduction in submergence depth $h_S = 0.191$, it is observed that metastable states appear at a higher depth in this case

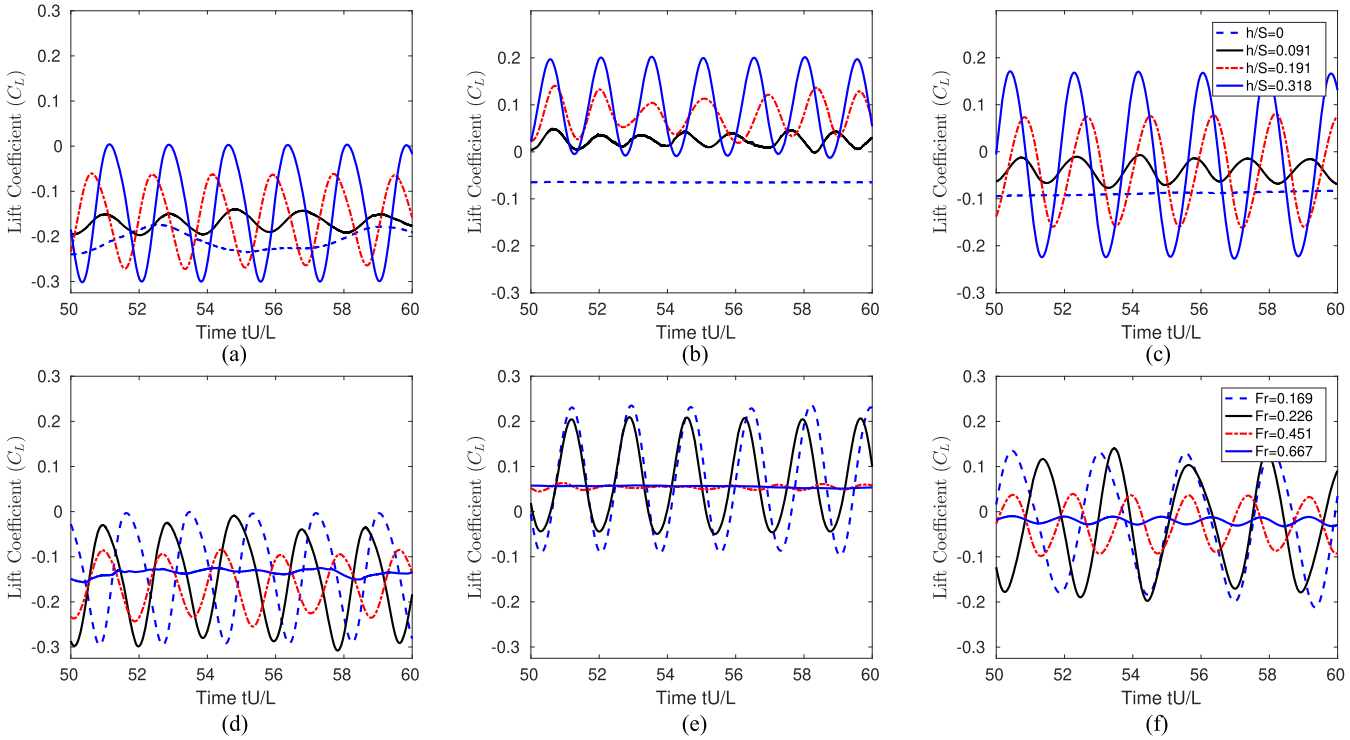

FIG. 10. Variation of C_L with depth (top) and Froude number (bottom) for AR = 2. (a) $\alpha = -45°$, (b) $\alpha = 45°$, (c) $\alpha = 90°$, (d) $\alpha = -45°$, (e) $\alpha = 45°$, and (f) $\alpha = 90°$.

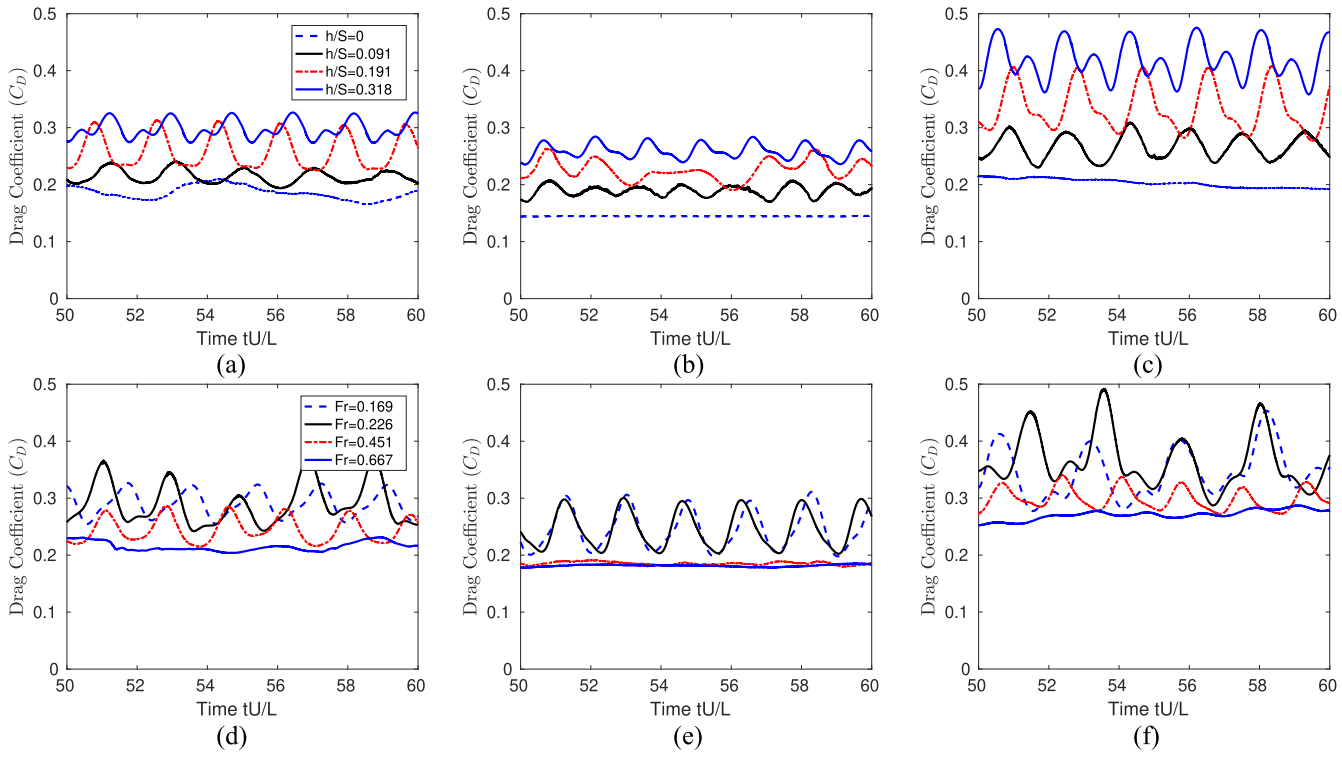

FIG. 11. Variation of C_D with depth (top) and Froude number (bottom) for AR = 2. (a) $\alpha = -45°$, (b) $\alpha = 45°$, (c) $\alpha = 90°$, (d) $\alpha = -45°$, (e) $\alpha = 45°$, and (f) $\alpha = 90°$.

than the one observed at $\alpha = 45°$. Increasing the proximity of the cylinder towards the free surface ($h_S = 0.096$) results in vortex shedding suppression. This is not observed for the other AOAs. The reason for this increased stabilization at $\alpha = 45°$ is discussed in the upcoming paragraphs. Finally at depth $h_S = 0$, the vortex shedding is suppressed where the angle of the shear

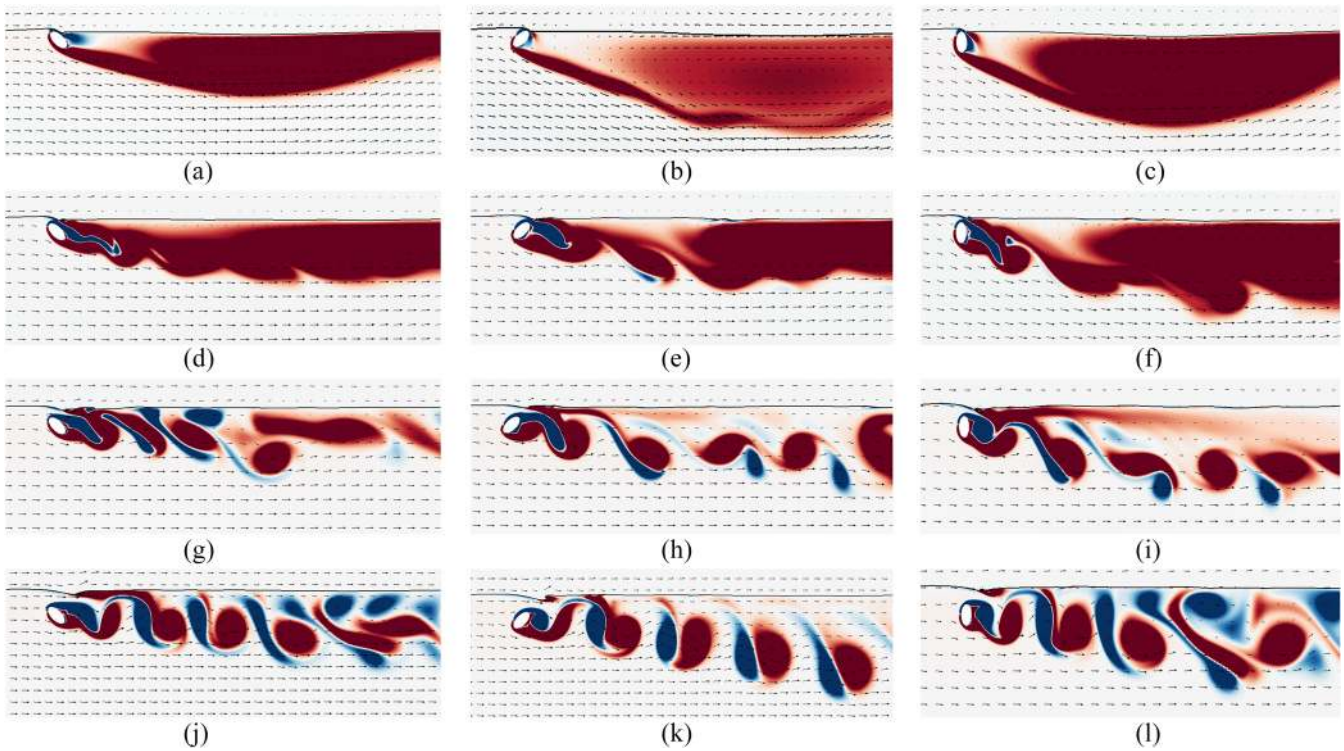

FIG. 12. Vorticity plots (−1 to 1) for different AOAs and depths at tU/S = 60 and $Fr = 0.338$. (a) $h_S = 0$, $\alpha = 45°$; (b) $h_S = 0$, $\alpha = -45°$; (c) $h_S = 0$, $\alpha = 90°$; (d) $h_S = 0.096$, $\alpha = 45°$; (e) $h_S = 0.096$, $\alpha = -45°$; (f) $h_S = 0.096$, $\alpha = 90°$; (g) $h_S = 0.191$, $\alpha = 45°$; (h) $h_S = 0.191$, $\alpha = -45°$; (i) $h_S = 0.191$, $\alpha = 90°$; (j) $h_S = 0.318$, $\alpha = 45°$; (k) $h_S = 0.318$, $\alpha = -45°$; and (l) $h_S = 0.318$, $\alpha = 90°$.

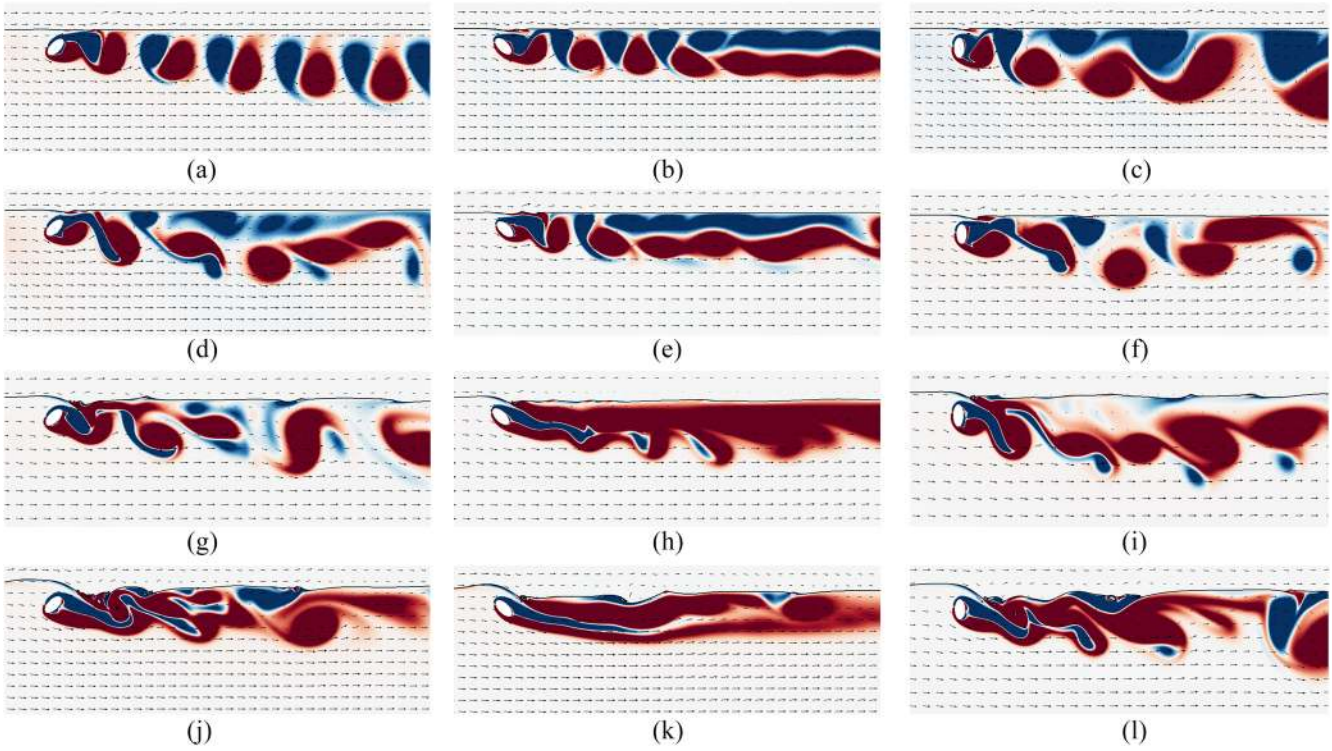

FIG. 13. Vorticity plots (−1 to 1) for different AOAs and Froude numbers at tU/S = 60 and h_S = 0.171. (a) Fr = 0.169, α = −45°; (b) Fr = 0.169, α = 45°; (c) Fr = 0.169, α = 90°; (d) Fr = 0.226, α = −45°; (e) Fr = 0.226, α = 45°. (f) Fr = 0.226, α = 90°; (g) Fr = 0.451, α = −45°; (h) Fr = 0.451, α = 45°; (i) Fr = 0.451, α = 90°; (j) Fr = 0.667, α = −45°; (k) Fr = 0.667, α = 45°; and (l) Fr = 0.667, α = 90°.

layer is less than that of the former AOA case [Fig. 12(a)]. When we vary the Froude number at a depth h_S = 0.176, the flow stabilizes very soon at a Froude number Fr = 0.451 for this AOA, and the jet stays unperturbed for a longer length due to negative vorticity sandwiched between two positive vortices.

3. Angle of attack = 90°

When the elliptic cylinder is oriented at α = 90°, vortex shedding occurs. The negative vorticity gets stretched by the shear layer and disintegrates into two blobs, which is similar to the flow with α = 45°. Further approach towards the free surface skews the near wake shedding at h_S = 0.191 and then it gets partially suppressed at h_S = 0.096. The variation in wake characteristics with the Froude number is the same as that in other AOAs, except at Fr = 0.226, where two flow states appear. These states are similar to metastable states in mechanism, but each state lasts only for 1-2 cycles before transition.

4. Jet from top of cylinder

As shown by Sheridan *et al.*[3] and Reichl *et al.*,[4] the jet from the top of the cylinder flows at an angle depending on the depth of the submergence and Froude number. At lower depths and higher Froude numbers, deformation in the free surface is significant enough to deflect the jet to a higher angle producing a shear layer behind the body. This layer, being the main cause for stretching and separation of vortices, reduces in size as submergence depth increases. The angle of the jet is also observed to decrease with the increase in submergence depth (h_S) since the effect of the free surface reduces. The size of the recirculation region, enclosed between the jet and hind-surface of the cylinder, depends on AOA and h_S. When an elliptic cylinder is placed at α = 45°, the size of the recirculation zone is limited by the free surface, and the adverse pressure gradient behind the cylinder is small. It can be said that this recirculation zone, being the source for low pressure, pulls the shear layer from beneath the cylinder upwards and causes vortex shedding. Specifically at a depth h_S = 0.096, the recirculation zone disappears because the jet stays in contact with the hind surface of the cylinder leaving no space, and with no low pressure zone, it follows with the suppression of wake instabilities. When h_S increases to 0.191, the angle of jet reduces, offering relatively more space for the recirculation zone. So, the jet alternates between sticking close to the free surface and flowing at an angle. Finally at h_S = 0.318, the recirculation zone is large enough for vortex shedding. At α = −45°, recirculation zone size is the largest when placed near a free surface, as more space is present between the jet and hind surface of the cylinder. The adverse pressure gradient introduced due to the hind surface of the cylinder (faces away from the free surface) is high. Therefore even at a smaller depth h_S = 0.096, vortex shedding, being one of the metastable states, is a natural occurrence at this AOA. At α = 90° and depth h_S = 0.096, oscillations are observed along with vortex shedding suppression because the recirculation region is moderate in size.

5. Flow regimes

Figure 14 shows the different regimes for the flow past elliptic cylinder with aspect ratios AR = 2 and 4. Figure 14(a) shows that the occurrence of metastable states is delayed for α = 45° at a moderate submergence depth (h_S = 0.191), whereas for α = −45°, it happens at h_S = 0.096. At Fr = 0.338,

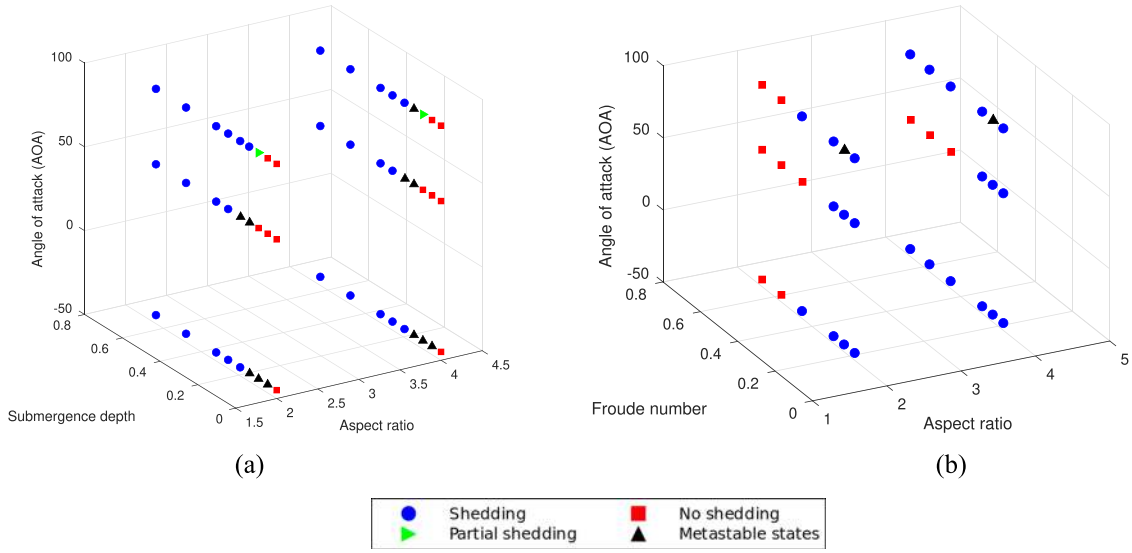

FIG. 14. Different flow regimes. (a) Depth and (b) Froude number.

flow regimes remain the same for both the aspect ratios. The aspect ratio does not influence the flow characteristics except at $Fr = 0.667$, where vortex shedding occurs with the increase in aspect ratio AR = 4.

B. Mean forces

Variation of mean forces with AOA and AR is shown in Fig. 15. The trends in the variation are explained using the dimensionless pressure (C_p) distribution on the elliptic cylinder for AR = 2 and 4.

1. AR = 2

Mean force coefficients, $\overline{C_L}$ and $\overline{C_D}$, of the elliptic cylinder with AR = 2 are studied. As shown in Fig. 15(b), the Froude number does not affect the mean lift ($\overline{C_L}$) but reduces the lift amplitude, which is caused by the free-surface's ability to stabilize the jet emanating from above the elliptic cylinder. Approaching the body towards the free surface reduces $\overline{C_L}$, as shown in Fig. 15(a). Especially for $\alpha = 45°$, $\overline{C_L}$ turns negative at low submergence depths. This reduction in $\overline{C_L}$ with decreasing depth is caused by the movement of the

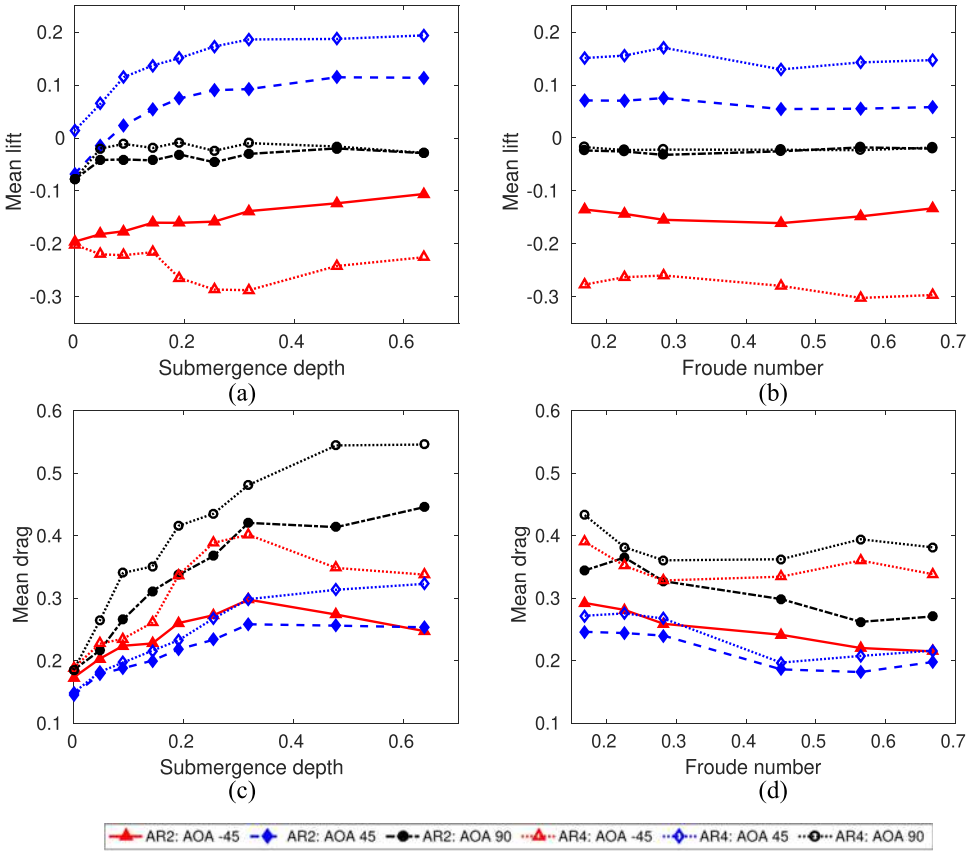

FIG. 15. Comparison of forces for different aspect ratios.

stagnation pressure point (SPP) on the surface of the elliptic cylinder upwards. Basic observations on $\overline{C_D}$ are summarized as follows: $\overline{C_D}$ of an elliptic cylinder decreases with its approach towards the free surface and an increase in the Froude number.

2. AR = 4

$\overline{C_L}$ increases with increasing AR, and its rate of change with increasing aspect ratio at 45° is higher than that at 90°. $\overline{C_L}$ at $\alpha = -45°$ becomes less negative (reduces in magnitude) at lower depths which is in contrast to the corresponding AR = 2 case. Changes in the Froude number do not significantly affect $\overline{C_L}$. $\overline{C_D}$ increases in magnitude with rising submergence depth and aspect ratio. Similar to the previous AR case, $\overline{C_D}$ is the lowest at $\alpha = 45°$ but with less difference in $\overline{C_D}$ brought by varying AR and is the highest at $\alpha = 90°$. When examined for the effect of the Froude number, $\overline{C_D}$ decreases with increasing Froude number, which is the same as observed in AR = 2. As stated before, the perimeter of the elliptic cylinder with different ARs is kept constant, so the frontal area is higher for cylinders with larger aspect ratios. As a result, the magnitude of mean forces acting on the elliptic cylinder of AR = 4 is generally higher.

3. Pressure acting on cylinder

Dimensionless pressure acting on the bluff body (C_p) is analyzed to explain the behavior of $\overline{C_D}$ and $\overline{C_L}$ for AR = 2, as shown in Fig. 16. C_p used in the figure is not absolute but relative. C_p is obtained by subtracting it with hydrostatic pressure to remove gravity or buoyancy effects with the assumption that buoyancy force balances the weight of the body. Thus C_p is influenced by the fluid flow and curvature of the free surface. The curvature introduces an imbalance in the hydrostatic pressure resulting in a net force, and this net force is significant at lower depths and Froude numbers. This effect is observed for a cylinder of $\alpha = 45°$, where increasing the Froude number from 0.169 to 0.226 increases $\overline{C_L}$. The counter-clockwise direction is taken as the convention for angles and the horizontal line pointing along the flow direction as the zeroth angle. At $h_S = 0.318$, two high C_p regions appear on the cylinder with $\alpha = -45°$ at the instant of maximum lift ($t = t_{max}$): one at roughly −2.8 rad (near leading edge) and other at −0.5 rad (hind side) but of lower magnitude. The high pressures at these points are the main source for high drag and low lift when compared with other submergence depths. But at the instant of minimum lift ($t = t_{min}$), the maximum pressure at −0.5 rad disappears reducing the lift as a result. For the cylinder with $\alpha = 45°$, there is a maximum in C_p at roughly 2.5 rad and $t = t_{max}$, which results in a net positive lift and drag. At $t = t_{min}$, C_p maximum appears roughly at 0.25 rad (the hind side of the cylinder), which reduces the net positive lift resulting in a lift minimum. For an elliptic cylinder with $\alpha = 90°$ and at $t = t_{max}$, pressure extrema appear at 1.5 and −1.5 rad because flow over the cylinder is maximum at this instant. At $t = t_{min}$, the C_p curve is mirror opposite of the one obtained at $t = t_{max}$ that is expected at higher depths. When the elliptic cylinder approaches the free surface ($h_S = 0.191$), the C_p profile changes substantially. With $\alpha = -45°$, the C_p maximum that was present in the previous submergence case disappears completely at $t = t_{max}$, while another C_p maximum develops roughly at 3 rad. These two factors are responsible for the reduction in the mean drag and lift. Reduction in the lift occurs for $\alpha = 45°$ due to a low-pressure zone developing roughly at −1 rad (near trailing edge). We observe asymmetry in C_p for the body with $\alpha = 90°$ at a depth of $h_S = 0.191$. In general, SPP moves upwards when the cylinder is moved closer to the free surface at all AOA. The direction of the normal at that point gains a vertical component in the −ve y-direction while losing its horizontal component, being the main reason behind the previously stated behavior of $\overline{C_L}$ and $\overline{C_D}$. For AR = 4, C_p is observed to increase on the hind surface of the elliptic cylinder oriented at $\alpha = -45°$ with the increasing proximity to the free surface (Fig. 17). The increased pressure behind the cylinder reduces the magnitude of $\overline{C_L}$.

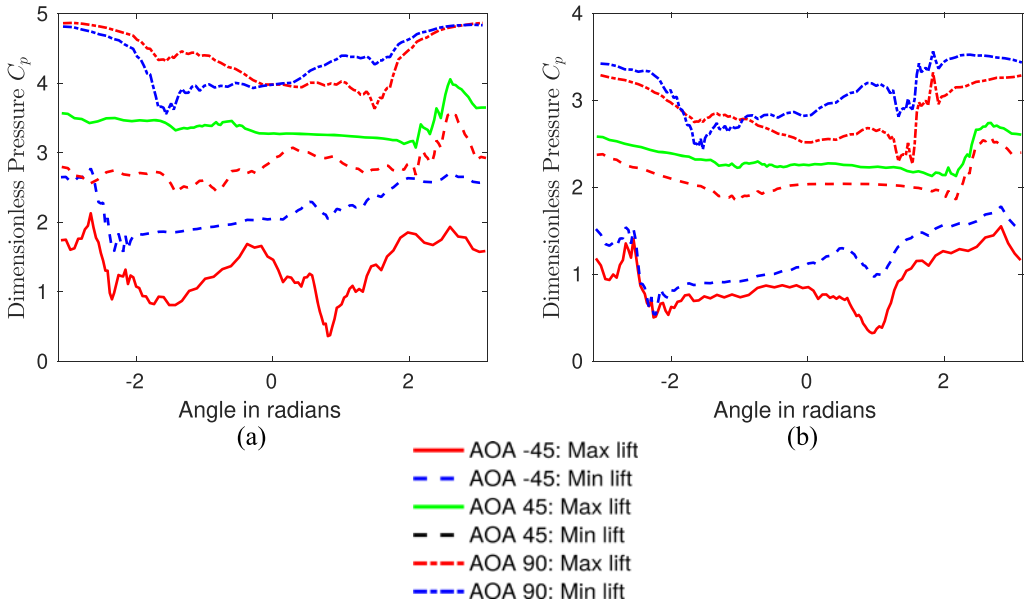

FIG. 16. C_p on the body at different AOAs for AR = 2. (a) $h_S = 0.318$ and (b) $h_S = 0.191$.

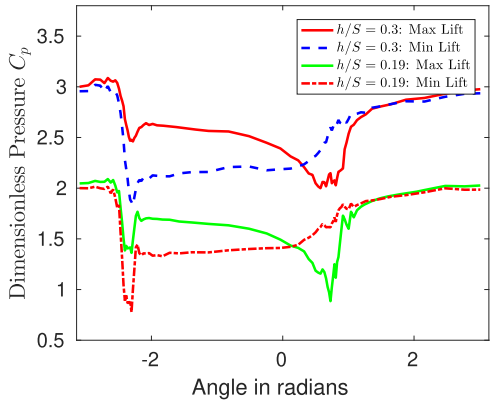

FIG. 17. C_p on the body at $\alpha = -45°$ for AR = 4.

C. Flow above the cylinder

To explain and quantify the flow characteristics at different AOA and aspect ratios, it is necessary to evaluate the time-averaged and height-averaged x-velocity on top of the cylinder denoted by $\bar{\bar{u}}$. It has a great impact on flow characteristics and other parameters such as the Strouhal number. Even though, it is tempting to use height-averaged velocity at the instant of maximum lift, as pointed out in the work of Reichl *et al.*,[4] the variation in geometry (AOA and AR) demands a different treatment for quantifying the flow above the elliptic cylinder. For most of the cases, maximum in the lift does not essentially correspond in time to the maximum in average flow above the cylinder. Thus, there is a need to average the quantity in time too. This quantity can be used to get an estimate of the fluid transport even for the cases with no vortex shedding.

1. AR = 2

We obtain $\bar{\bar{u}}$ for a different h_S and Froude number and plot it in Fig. 18. We can observe the following about $\bar{\bar{u}}$ for AR = 2:

(a) Increasing the Froude number decreases $\bar{\bar{u}}$ irrespective of AOA.
(b) Increasing the depth increases $\bar{\bar{u}}$ irrespective of AOA because there is less hindrance to fluid flow at higher submergence depths.
(c) The influence of orientation on $\bar{\bar{u}}$ is best demonstrated by comparing elliptic cylinders oriented at $\alpha = 45°$ and $-45°$, as shown in Fig. 9. An elliptic cylinder with $\alpha = 45°$ allows the least $\bar{\bar{u}}$ irrespective of the Froude number or submergence depth, while the one with $\alpha = -45°$ has a relatively higher $\bar{\bar{u}}$. This dependence of $\bar{\bar{u}}$ on orientation is due to fluid preferring the easier path. So with $\alpha = -45°$, fluid-flow follows the upper portion of the cylinder resulting in an increase in $\bar{\bar{u}}$. It is observed that, for $\alpha = 90°$, higher $\bar{\bar{u}}$ values result for a wider range of Froude numbers (at $h_S = 0.171$) and submergence depths compared to other AOAs. Higher $\bar{\bar{u}}$ for elliptic cylinders inclined at $\alpha = 90°$ results from the higher frontal area, which exhibits the natural ability to collect a higher amount of incident fluid flow.

2. AR = 4

Flow above the cylinder ($\bar{\bar{u}}$) is observed to reduce with increasing aspect ratio (AR = 4). Such results are counter-intuitive as the rise in the frontal area, brought by the increasing aspect ratio, does not achieve higher $\bar{\bar{u}}$ but the opposite. Figures 19 and 20 support these observations, where the number of streamlines incident on the elliptic cylinder of higher AR reduces on top of the cylinder. Out of the three AOAs, $\bar{\bar{u}}$ is the highest with $\alpha = -45°$ for a wide range of Froude numbers and submergence ratios ($h_S > 0.1$) because the fluid tends to move upwards when subjected to an elliptic cylinder inclined at $\alpha = -45°$. It is clearly displayed for flow with a low Froude number ($Fr = 0.169$), where there is a large disparity between $\bar{\bar{u}}$ values for $\alpha = -45°$ and other AOAs. Increasing the Froude number brings the $\bar{\bar{u}}$ for the three AOAs closer, signifying that $\bar{\bar{u}}$ stays the highest with $\alpha = 45°$ due to its geometry and less free-surface deformation (at low Froude number). It is in contrast to the corresponding AR = 2 case. In Fig. 18(a), it is observed that $\bar{\bar{u}}$ for $\alpha = 90°$ is higher at lower submergence depths and it changes to a minimum when the depth is increased to $h_S = 0.191$ or higher. With $\alpha = -45°$, $\bar{\bar{u}}$ stays at a minimum at lower submergence depths ($h_S < 0.1$) and maximum at higher submergence depths. It is noted that for $\alpha = 45°$ and $\alpha = 90°$, $\bar{\bar{u}}$ drops less with higher deformation (or proximity to free surface) compared to that for $\alpha = -45°$.

3. Wave breaking

Flow above the cylinder also determines the wave breaking phenomena. Wave breaking, a source for the substantial

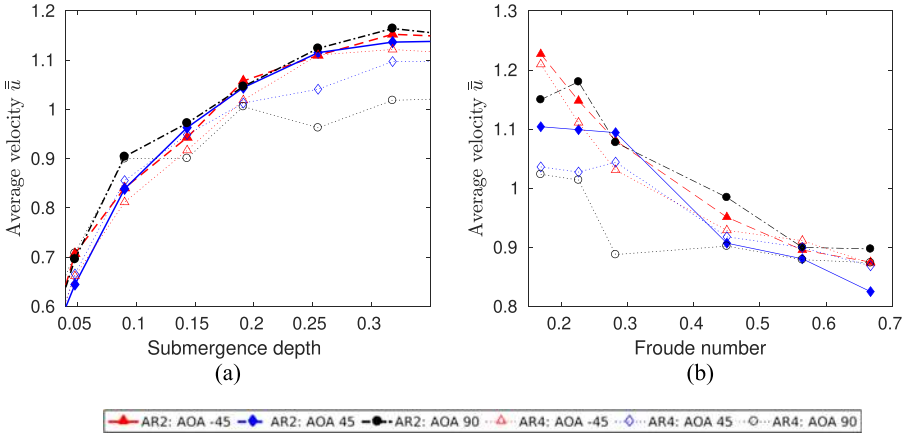

FIG. 18. Variation of average velocity above the cylinder.

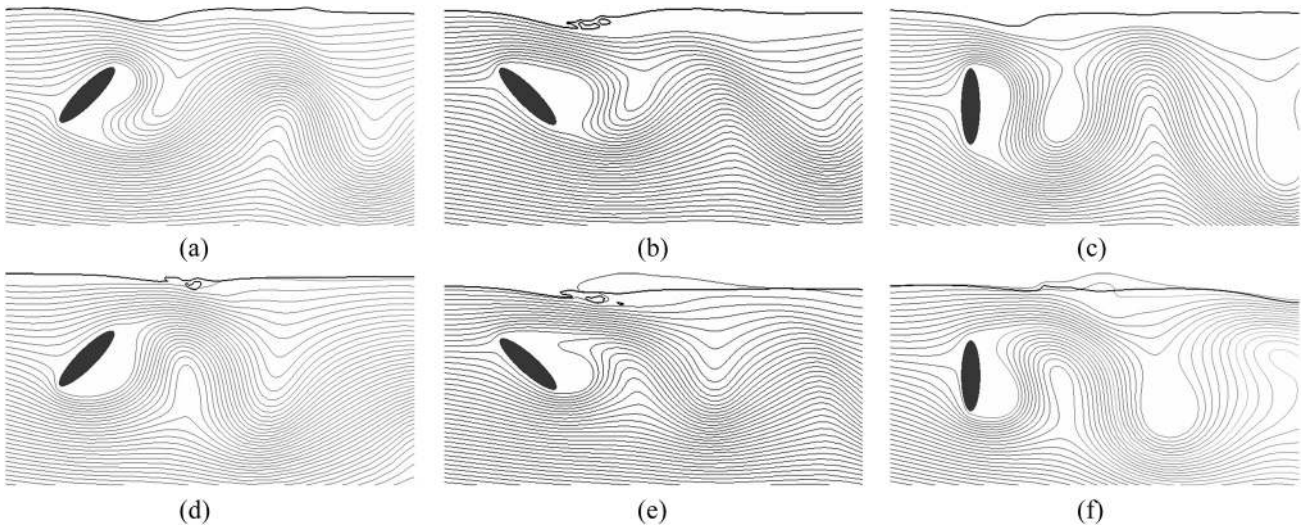

FIG. 19. Streamlines for AR = 4 at $h_S = 0.318$. (a) $\alpha = -45°$, maximum C_L, (b) $\alpha = 45°$, maximum C_L, (c) $\alpha = 90°$, maximum C_L, (d) $\alpha = -45°$, minimum C_L, (e) $\alpha = 45°$, minimum C_L, and (f) $\alpha = 90°$, minimum C_L.

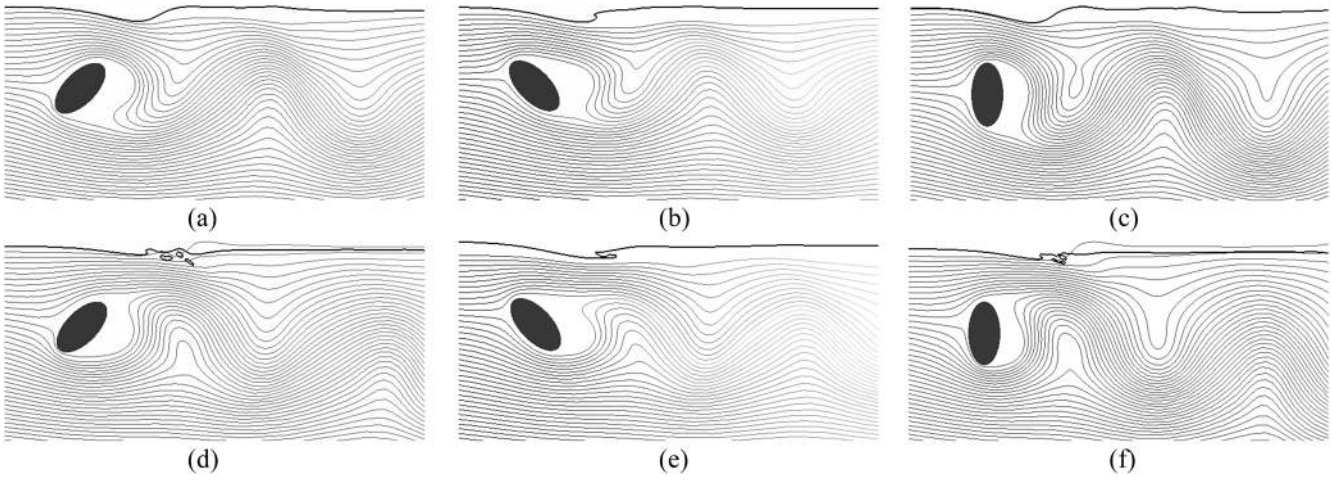

FIG. 20. Streamlines for AR = 2 at $h_S = 0.318$. (a) $\alpha = -45°$, maximum C_L, (b) $\alpha = 45°$, maximum C_L, (c) $\alpha = 90°$, maximum C_L, (d) $\alpha = -45°$, minimum C_L, (e) $\alpha = 45°$, minimum C_L, and (f) $\alpha = 90°$, minimum C_L.

amount of vorticity, is influenced by the local Froude number that is defined as $Fr_L = \bar{u}/\sqrt{gL}$. Wave breaking happens when the local Froude number exceeds unity ($Fr_L > 1$). The maximum of Fr_L, which utilizes the maximum in average velocity above the cylinder ($\bar{u}_m$) as its velocity scale, is plotted in Fig. 21. Fr_L attained for $\alpha = -45°$ and 90° is higher

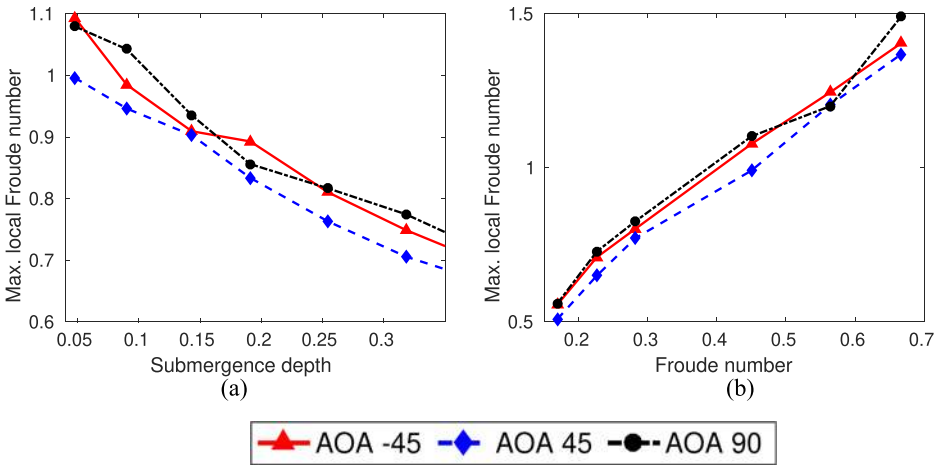

FIG. 21. Maximum local Froude number at AR = 2. (a) $Fr = 0.338$ and (b) $h_S = 0.175$.

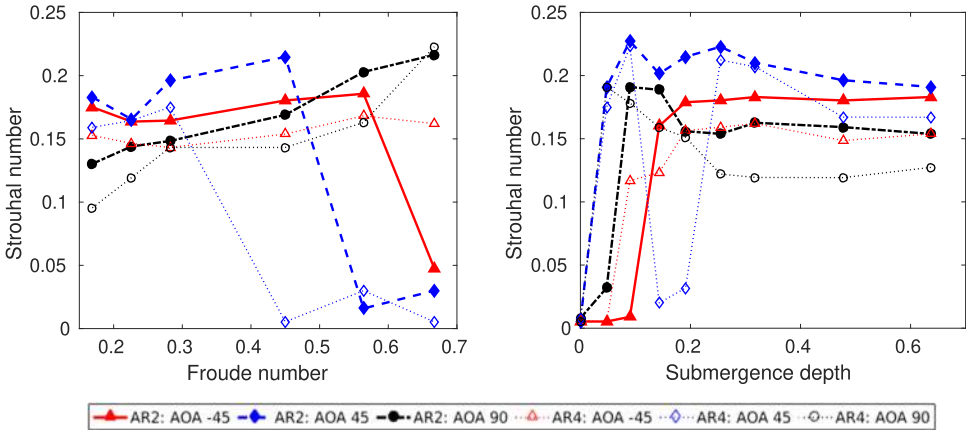

FIG. 22. Variation of the Strouhal number.

than Fr_L for $\alpha = 45°$, which sets the difference in their shedding patterns, as shown in Fig. 9. The vorticity induced by wave breaking causes the jet above the cylinder to travel at an angle.

D. Strouhal number

AOA has a large impact on the Strouhal number (St). The variation in fundamental frequencies of the vertical force with the submergence depth and Froude number is plotted in Fig. 22. For the cases that exhibit metastable states, the frequency of the state in which shedding occurs is plotted. The trend of increasing Strouhal number with $\bar{\bar{u}}$ is observed for $\alpha = -45°$. In spite of using $\bar{\bar{u}}$ instead of $\bar{u}$, it is still in agreement with the arguments made by Reichl *et al.*[4] But the same argument cannot be used to explain the major differences in frequencies for flow with other AOAs. The Strouhal number for $\alpha = -45°$ is the highest amongst other AOAs for all depths because the bottom shear layer takes lesser time, compared to other AOAs, to meet the jet emanating from the top part of the cylinder. In contrary to the trend seen in other AOA cases, St for $\alpha = 45°$ decreases with increasing depth since the angle, at which jet flows, changes substantially with h_S. Thus irrespective of the increase in $\bar{\bar{u}}$ for this particular AOA, St decreases with increasing proximity to the free surface, as the bottom shear layer gets far from the jet, and yet it is close enough compared to other AOAs (Fig. 23).

1. AR = 2

For $\alpha = 45°$, St is high at all submergence depths, with a peak at $h_S = 0.096$ where shedding is suppressed. Even with suppression, the oscillations in forces originate from the body's proximity to the free surface and wave breaking. A peak in the Strouhal number is observed for $\alpha = 45°$ at $h_S = 0.096$, where partial vortex-shedding suppression and a recirculation zone is observed. A slight increase in fundamental frequency is seen for $\alpha = -45°$ after $h_S = 0.096$. This is mainly caused by the increase in $\bar{\bar{u}}$. Since elliptic cylinders with $\alpha = 45°$ and $-45°$ cause mirror image flows without the free surface, St is expected to meet each other at higher h_S values (>1). The reason behind the shedding frequency for $\alpha = 45°$ to be high was stated in the previous paragraph. For $\alpha = 90°$, the frequency reaches a minimum at $h_S = 0.318$ after a peak at $h_S = 0.096$. This frequency is close to that reported in the work of Johnson.[19]

2. AR = 4

Figure 22 shows increasing frequency for the three AOAs with an increase in the Froude number. The sudden reduction in principal modes for $\alpha = 45°$ at a higher Froude number is clearly a sign of vortex-shedding suppression. As observed in Fig. 22, the principal modes decrease generally with an increase in the aspect ratio (AR) for a wide range of Froude numbers and submergence depths. This is caused due to the low $\bar{\bar{u}}$ for higher AR cases, as seen in Fig. 18. When examined for the effect of submergence depth on the Strouhal number, the trend is the same as that of AR = 2. For $\alpha = -45°$, there is a reduction in the principal mode with an increase in AR. This can be explained with the help of Fig. 24 that the shedding pattern (not the shedding angle) remains the same but $\bar{\bar{u}}$ is again lower for AR = 4. Reduction in $\bar{\bar{u}}$ causes a decline in the Strouhal number as the aspect ratio is increased. For $\alpha = 45°$, the frequencies stay high in comparison to other AOA (similar to the AR = 2 case). The maxima (at $h_S = 0.096$) increase with increasing aspect ratio. For $\alpha = 90°$, shedding frequency reduces with increasing aspect ratio, at $h/S > 0.191$. This is in agreement with the work of Radi *et al.*,[38] where the Strouhal number reduces with an increase in AR. It can be concluded that parameters like AOA and AR play an important role in determining the Strouhal number.

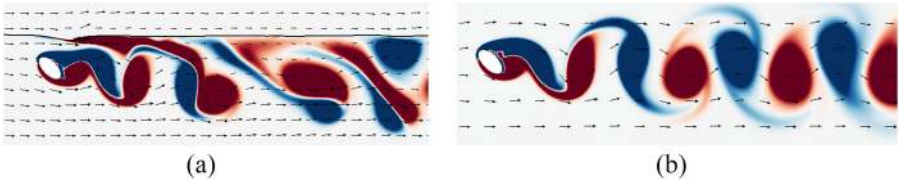

FIG. 23. Comparison of vortex shedding for cases with and without interface. (a) AOA = 45° and (b) unbounded case.

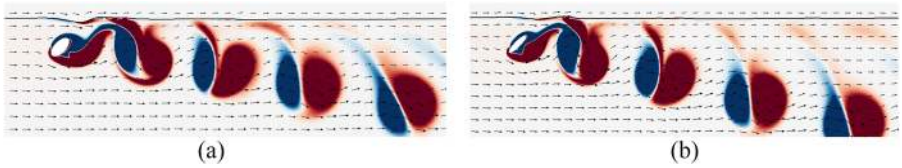

FIG. 24. Shedding for different ARs with $\alpha = -45°$. (a) AR = 2, $\alpha = -45°$ and (b) AR = 4, $\alpha = -45°$.

VII. CONCLUSIONS

The elliptic cylinder with different aspect ratios (ARs) and angles of attack (AOAs) was examined as the submergence depth (h_S) and Froude number (Fr) are varied. Even though the flow around elliptic cylinders inclined at 45° and −45° is equal and opposite, flow characteristics change drastically in the presence of a free surface. The most obvious of all the changes in flow brought by elliptic cylinders is that an elliptic cylinder with AOA = 45° exhibits tendency to suppress vortex shedding in the flow and maintains an undisturbed jet under the influence of the free surface at lower depths and high Froude numbers, but with AOA = −45°, it fails to do the same. An elliptic cylinder with AOA = 90° causes partial vortex shedding suppression for both aspect ratios at $h_S = 0.096$, but fails to do the same at a higher Froude number. Another difference in the flow feature is observed at higher submergence depths and low Froude numbers. The shed vortices stick close to the free-surface for AOA = 45°, while for AOAs = −45° and 90°, the vortices move away from the free surface. When we study the mean forces acting on the body, it is found that the elliptic cylinder with AOA = 90° experiences the highest drag, while for AOA = 45°, the lowest drag is observed with the highest positive lift. Mean drag is observed to increase with rise in submergence depth for all AOAs, which is in agreement with that of Miyata.[1] The Strouhal number for flow with AOA = 45° decreases with an increase in depth, as opposed to the trend observed for other AOAs as well as in the work of Reichl *et al.*[4] It is due to the massive change in the flow pattern when depth is varied. Variation in AR does not affect the flow features significantly, but increasing AR increases the mean forces and reduces the Strouhal number globally. So it is concluded that the angle of attack and aspect ratio are important factors that determine the flow past an elliptic cylinder near a free surface. In the future, the influence of more parameters will be explored.

[1]H. Miyata, N. Shikazono, and M. Kanai, "Forces on a circular cylinder advancing steadily beneath the free-surface," Ocean Eng. **17**, 81 (1990).
[2]G. S. Triantafyllou and A. A. Dimas, "Interaction of two dimensional separated flows with a free surface at low Froude numbers," Phys. Fluids A **1**, 1813 (1989).
[3]J. Sheridan, J.-C. Lin, and D. Rockwell, "Flow past a cylinder close to a free surface," J. Fluid Mech. **330**, 1 (1997).
[4]P. Reichl, K. Hourigan, and M. C. Thompson, "Flow past a cylinder close to a free surface," J. Fluid Mech. **533**, 269 (2005).
[5]B. Bouscasse, A. Colagrossi, S. Marrone, and A. Souto-Iglesias, "SPH modelling of viscous flow past a circular cylinder interacting with a free surface," Comput. Fluids **146**, 190 (2017).
[6]S. Taneda, "Experimental investigation of vortex streets," J. Phys. Soc. Jpn. **20**, 1714 (1965).
[7]P. W. Bearman and M. M. Zdravkovich, "Flow around a circular cylinder near a plane boundary," J. Fluid Mech. **89**, 33–47 (1978).
[8]S.-J. Lee, S.-I. Lee, and C.-W. Park, "Reducing the drag on a circular cylinder by upstream installation of a small control rod," Fluid Dyn. Res. **34**, 233 (2004).
[9]A. Dipankar and T. Sengupta, "Flow past a circular cylinder in the vicinity of a plane wall," J. Fluids Struct. **20**, 403 (2005).
[10]A. Rao, B. Stewart, M. Thompson, T. Leweke, and K. Hourigan, "Flows past rotating cylinders next to a wall," in *IUTAM Symposium on Bluff Body Wakes and Vortex-Induced Vibrations (BBVIV-6)* [J. Fluids Struct. **27**, 668 (2011)].
[11]A. Rao, M. Thompson, T. Leweke, and K. Hourigan, "The flow past a circular cylinder translating at different heights above a wall," J. Fluids Struct. **41**, 9 (2013), special issue on Bluff Body Flows (Blubof2011).
[12]K. Shaafi and S. Vengadesan, "Wall proximity effects on the effectiveness of upstream control rod," J. Fluids Struct. **49**, 112 (2014).
[13]Y. Xia, J. Lin, X. Ku, and T. Chan, "Shear-induced autorotation of freely rotatable cylinder in a channel flow at moderate Reynolds number," Phys. Fluids **30**, 043303 (2018).
[14]H. J. Lugt and H. J. Haussling, "Laminar flow past an abruptly accelerated elliptic cylinder at 45 incidence," J. Fluid Mech. **65**, 711–734 (1974).
[15]J. K. Park, S. O. Park, and J. M. Hyun, "Flow regimes of unsteady laminar flow past a slender elliptic cylinder at incidence," Int. J. Heat Fluid Flow **10**, 311 (1989).
[16]H. M. Badr, S. C. R. Dennis, and S. Kocabiyik, "Numerical simulation of the unsteady flow over an elliptic cylinder at different orientations," Int. J. Numer. Methods Fluids **37**, 905 (2001).
[17]K. Shintani, A. Umemura, and A. Takano, "Low Reynolds-number flow past an elliptic cylinder," J. Fluid Mech. **136**, 277 (2006).
[18]Z. Faruquee, D. S. Ting, A. Fartaj, R. M. Barron, and R. Carriveau, "The effects of axis ratio on laminar fluid flow around an elliptical cylinder," Int. J. Heat Fluid Flow **28**, 1178 (2007).
[19]S. Johnson, "Flow past elliptical cylinders at low Reynolds numbers," in *14th Australasian Fluid Dynamics Conference*, edited by B. Dally (Adelaide University, 2001), Vol. 1, p. 343.
[20]S. A. Johnson, M. C. Thompson, and K. Hourigan, "Predicted low frequency structures in the wake of elliptical cylinders," Eur. J. Mech. B: Fluids **23**, 229 (2004).
[21]I. Paul, K. Arul Prakash, and S. Vengadesan, "Onset of laminar separation and vortex shedding in flow past unconfined elliptic cylinders," Phys. Fluids **26**, 023601 (2014).
[22]I. Paul, K. A. Prakash, S. Vengadesan, and V. Pulletikurthi, "Analysis and characterisation of momentum and thermal wakes of elliptic cylinders," J. Fluid Mech. **807**, 303 (2016).
[23]Daichin and S. J. Lee, "Near-wake flow structure of elliptic cylinders close to a free surface: Effect of cylinder aspect ratio," Experiments in Fluids **36**, 748 (2004).
[24]S. N. Naik, S. Vengadesan, and K. A. Prakash, "Numerical study of fluid flow past a rotating elliptic cylinder," J. Fluids Struct. **68**, 15 (2017).
[25]N. Srinidhi and S. Vengadesan, "Ground effect on tandem flapping wings hovering," Comput. Fluids **152**, 40 (2017).
[26]R. Mittal and G. Iaccarino, "Immersed boundary methods," Annu. Rev. Fluid Mech. **37**, 239 (2005).
[27]K. Taira and T. Colonius, "The immersed boundary method: A projection approach," J. Comput. Phys. **225**, 2118 (2007).
[28]Z. Chen, C. Shu, and D. Tan, "Immersed boundary-simplified lattice boltzmann method for incompressible viscous flows," Phys. Fluids **30**, 053601 (2018).
[29]J. A. Sethian, "Evolution, implementation, and application of level set and fast marching methods for advancing fronts," J. Comput. Phys. **169**, 503 (2001).
[30]G.-S. Jiang and D. Peng, "Weighted ENO schemes for Hamilton–Jacobi equations," SIAM J. Sci. Comput. **21**, 2126 (2000).
[31]M. Sussman, P. Smereka, and S. Osher, "A level set approach for computing solutions to incompressible two-phase flow," J. Comput. Phys. **114**, 146 (1994).
[32]S. Balay, S. Abhyankar, M. F. Adams, J. Brown, P. Brune, K. Buschelman, L. Dalcin, V. Eijkhout, W. D. Gropp, D. Kaushik, M. G. Knepley, D. A. May, L. C. McInnes, R. T. Mills, T. Munson, K. Rupp, P. Sanan,

B. F. Smith, S. Zampini, H. Zhang, and H. Zhang, PETSc Web page, http://www.mcs.anl.gov/petsc, 2018.
[33]Y. Saad and M. H. Schultz, "GMRES: A generalized minimal residual algorithm for solving nonsymmetric linear systems," SIAM J. Sci. Stat. Comput. **7**, 856 (1986).
[34]M. Adams, "Evaluation of three unstructured multigrid methods on 3d finite element problems in solid mechanics," Int. J. Numer. Methods Eng. **55**, 519 (2002).
[35]S. Popinet and S. Zaleski, "A front-tracking algorithm for accurate representation of surface tension," Int. J. Numer. Methods Fluids **30**, 775 (1999).
[36]S. Hysing, S. Turek, D. Kuzmin, N. Parolini, E. Burman, S. Ganesan, and L. Tobiska, "Quantitative benchmark computations of two-dimensional bubble dynamics," Int. J. Numer. Methods Fluids **60**, 1259 (2009).
[37]O. I. Gubanov, "Design of CFD code using high level programming paradigms: Free surface flows with arbitrarily moving rigid bodies," M.Sc. thesis, Memorial University of Newfoundland, 2007.
[38]A. Radi, M. C. Thompson, J. Sheridan, and K. Hourigan, "From the circular cylinder to the flat plate wake: The variation of Strouhal number with Reynolds number for elliptical cylinders," Phys. Fluids **25**, 101706 (2013).